Article

Interfacial reinforced carbon fiber composites inspired by biological interlocking structure

High mechanical performance

Yufei Wang,
Zhengzhi Mu,
Zhiyan Zhang, ...,
Shichao Niu,
Zhiwu Han,
Luquan Ren

zmu@jlu.edu.cn

Highlights

Natural HGMS and mechanical interlocking mechanism were carefully investigated

Biomimetic HGMS based on functionalized CFs and ZnO NRs was constructed

Mechanical performance of the bioinspired CFRCs was enhanced significantly

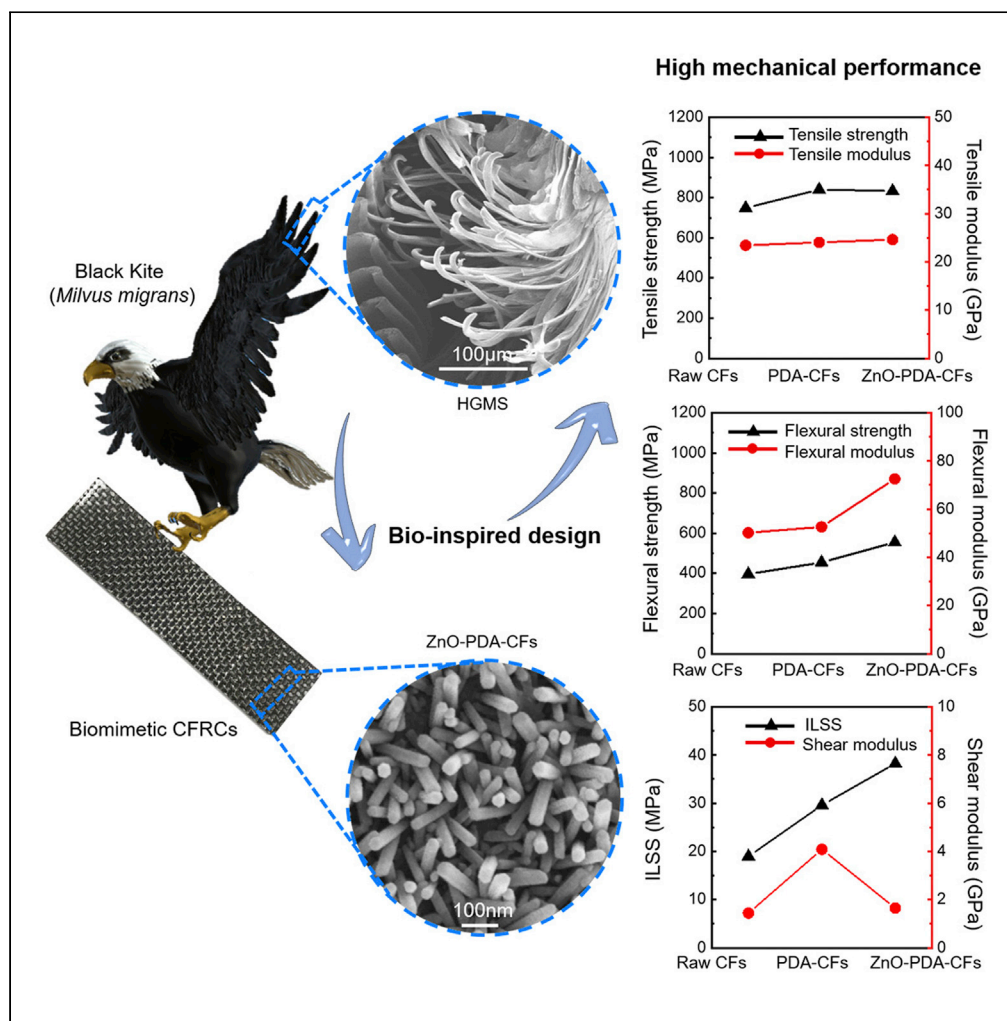The interface adhesion between the CFs and EP was proved to be enhanced

Article

Interfacial reinforced carbon fiber composites inspired by biological interlocking structure

Yufei Wang,[1] Zhengzhi Mu,[1,2,6,*] Zhiyan Zhang,[1] Wenda Song,[1] Shuang Zhang,[1] Handong Hu,[3,4] Zhe Ma,[3] Liewei Huang,[3] Dashun Zhang,[5] Ze Wang,[1,2] Yujiao Li,[1] Binjie Zhang,[1] Bo Li,[1,2] Junqiu Zhang,[1] Shichao Niu,[1] Zhiwu Han,[1] and Luquan Ren[1]

SUMMARY

Weak interfacial activity and poor wettability between fiber and matrix are known to be the two main factors that restrict the mechanical properties of carbon fiber-reinforced composites (CFRCs). Herein, inspired by high strength and toughness characteristics of wing feathers of Black Kite (*Milvus migrans*), natural hook-groove microstructure system (HGMS) and underlying mechanical interlocking mechanism were carefully investigated. Biomimetic HGMS based on dopamine-functionalized carbon fibers and ZnO nanorods were constructed successfully by a two-step modification method to enhance interfacial adhesion. Further, CFRCs featured with biomimetic HGMS were prepared by a vacuum-assisted contact molding method. Experimental results confirmed that flexural strength and interlaminar shear strength of the bioinspired CFRCs were effectively improved by 40.02 and 101.63%, respectively. The proposed bioinspired design strategy was proved to be flexible and effective and it was anticipated to provide a promising design approach and facile fabrication method for desirable CFRCs with excellent mechanical properties.

INTRODUCTION

As typical high mechanical performance carbon fiber-reinforced composites (CFRCs), carbon fibers (CFs)/ epoxy (EP) composites featured with light weight, strong toughness, and high stiffness have been widely used in aerospace, rail transit, engineering machinery, and many other engineering fields (Lin et al., 2019; Eyckens et al., 2020; Kim et al., 2020; Li et al., 2020a; Hung et al., 2018). Interface behavior between fibers and matrix is a key factor to form stable and reliable composites. To maximize the strength of CFs/EP composites, it is necessary to realize the stress transfer from polymer matrix to CFs (Hu et al., 2020; Fu et al., 2020; Abidin et al., 2019). Generally, raw CFs without surface treatment are smooth and chemically inert, resulting in poor interfacial adhesion between carbon fiber surface and polymer matrix. It makes the interfacial bonding strength of the final composite very low (Cheng et al., 2018a, 2018b; Nasser et al., 2019). In particular, these raw fibers could be easily peeled off or pulled out from polymer matrix under load, which seriously affects the load transfer from matrix to fiber and thereby impairs mechanical properties of the composites (Mittal et al., 2018; Liu et al., 2020; Li et al., 2016). Therefore, relatively poor interfacial property is still an open challenge to achieve satisfactory CFRCs with high mechanical properties (Wu et al., 2018, 2021; Zhang et al., 2020a; Beggs et al., 2015; Jia et al., 2019; Chen et al., 2016; Ma et al., 2019; Zhan et al., 2021; Garlof et al., 2016, 2017).

To solve weak interfacial adhesion of existing CFRCs, various approaches for surface modification of CFs were extensively investigated (Prakash and Rajadurai, 2017; He et al., 2021; Dai et al., 2011; Andideh and Esfandeh, 2016; Wang et al., 2019; Chukov et al., 2019; Sun et al., 2020; Sepe et al., 2018; Nie et al., 2017; Hu et al., 2018; Huan et al., 2020; Zhu et al., 2017; Zhang et al., 2020b; Fu et al., 2019). The main purpose of these strategies is to improve the interfacial bonding strength between fibers and the matrix by providing more physical contact for mechanical interlocking, thereby creating rich active groups or good wettability for chemical bonding (Karnati et al., 2020; Raphael et al., 2018; Sharma et al., 2014). Many methods for surface modification of CFs were proved to be effective, including sizing, coating (Sepe et al., 2018; Nie et al., 2017; Su et al., 2021; Acar et al., 2020), chemical grafting (Cheng et al., 2018a, 2018b; Nasser et al., 2019; Banerjee et al., 2021; Krushnamurty et al., 2016; Jia et al., 2021), oxidation

[1]Key Laboratory of Bionic Engineering, Ministry of Education, Jilin University, Changchun 130022, China

[2]School of Mechanical and Aerospace Engineering, Jilin University, Changchun 130022, China

[3]X Lab, Second Academy of CASIC, Beijing 100854, China

[4]School of Aeronautics and Astronautics, Shanghai Jiao Tong University, Shanghai 200240, China

[5]No. 55 Research Institute of China North Industries Group Corporation, Changchun 130012, China

[6]Lead contact

*Correspondence:
zmu@jlu.edu.cn

https://doi.org/10.1016/j.isci. 2022.104066

treatment (Prakash and Rajadurai, 2017; Dai et al., 2011; Andideh and Esfandeh, 2016; Wang et al., 2019; Chukov et al., 2019; Sun et al., 2020), adding nanoparticles (Lau et al., 2013; Yao et al., 2021; Liu et al., 2021; Kurtulus et al., 2021), etc. Unfortunately, strong acid or toxic polar organic reagent treatments are easy to cause defects on the fragile surface of CFs, sacrificing the inherent tensile strength of the CFs in some degree. Besides, other modification methods, such as plasma treatment, high-energy radiation, electrophoretic deposition, and electrochemical methods, are usually high-cost and low-efficiency, which are easy to cause chemical pollution and difficult to achieve large-scale preparation (Cheng et al., 2018b; Zhu et al., 2017). Therefore, to reduce damage to the inherent mechanical properties of fibers caused by chemical treatment, it is necessary to explore a facile method for fiber modification to improve the interface conditions of CFRCs, thereby enhancing their mechanical performance.

Nature is a huge storage of diversified biological materials that provides many near-perfect structural templates for novel design of high performance biomimetic composites (McCoy et al., 2018; Zhao and Fan, 2019; Zhang et al., 2018; Huang et al., 2019; Song et al., 2021; Jiao et al., 2020; Han et al., 2017; Niu et al., 2016). Owing to orderly hierarchical structures and rich interface interactions, many natural biological materials including pearl, bones, and lobster cuticle can exhibit excellent mechanical properties featured with high strength and toughness (Peng and Cheng, 2017; Peng et al., 2020; Meyers et al., 2013; Zhang et al., 2020c). Particularly, for birds in flight, in spite of the complex aerodynamic load, structural damage like fracture won't appear in their wing feathers which could benefit from the interlocking structure between microscale hook and groove (Kovalev et al., 2014; Sullivan et al., 2017a). Plenty of barbs form the entire wing feather through the uniform arrangement of barbules on both sides of the barb. It was found that adjacent barbules are not simply smooth contact, but they are also connected with each other through hook-like and groove-like microstructures on the barbules to form a mechanical interlocking system. The hook-groove microstructure system (HGMS) makes the load transfer to barbs thus ensuring the whole mechanical strength of the entire feather vane. Moreover, the elongation rate between adjacent barbs can reach 270% before separation and the separation force can remain at more than 80% of the initial value even after 1000 times of separation-repair circles (Sullivan et al., 2017b). Considering the unique hook-groove interlocking mechanism between adjacent wing feathers, it provides a strong clue to apply this for improving comprehensive mechanical properties of CFRCs.

Herein, inspired by high strength and toughness characteristics of wing feathers of Black Kite (*Milvus migrans*), the natural interlocking structure system was mimicked with a two-step modification method involving functionalization of CFs surface and hydrothermal growth of ZnO NRs. The modification method in this work was to be confirmed effective through the significantly improved mechanical properties of CFRCs. Firstly, the surface of original CFs was coated with a poly dopamine (PDA) layer to offer affluent active functional groups. To enhance interface strength by establishing a close mechanical linkage between fiber and resin, dense ZnO NRs grew well on the fiber surface by a hydrothermal method. Surface morphology and chemical composition of the modified CFs were carefully characterized. To examine mechanical properties of the fabricated bioinspired CFRCs, composite samples were fabricated by a vacuum-assisted contact molding (VACM) method. Then, combined with the fracture morphology, failure modes of CFRCs were deeply investigated. More importantly, the underlying mechanical enhancement mechanism of the bioinspired CFRCs based on HGMS was proposed and discussed.

RESULTS

Characterization and interlocking mechanism of natural HGMS

As a large raptor with body length of 54-69 cm, Black Kite (*M. migrans*) feeds mainly on birds, mice, rabbits, and other small animals (Figure 1A). It possesses excellent flying ability because of its strong wings covered with massive feathers, which enable it to find prey by hovering at high altitudes in the air. Here, wing feathers of Black Kite were selected as the biological prototype. At the macroscale, a feather basically consists of a central rachis and barbs orderly distributed on both sides, forming the feather vane with curved surface (Figure 1B). Similarly, it was found that fine barbules grow on both side of barbs, thereby forming typical hierarchical structures within the feather vane, which was fully confirmed by scanning electron microscopy (SEM) imaging from different views (Figures 1C–1F and S1A–S1D). More interestingly, adjacent barbs were tightly connected through an interlocking microstructure system formed by barbules from two different barbs (Figures 1C, 1D, S1A and S1B). In detail, on the distal side of the barb, hook-like structures were found in the barbules (Figures 1E and S1C), whereas on the proximal side, groove-like structures were found existing in the barbules (Figures 1F and S1D). To clearly illustrate the interlocking mechanism, a
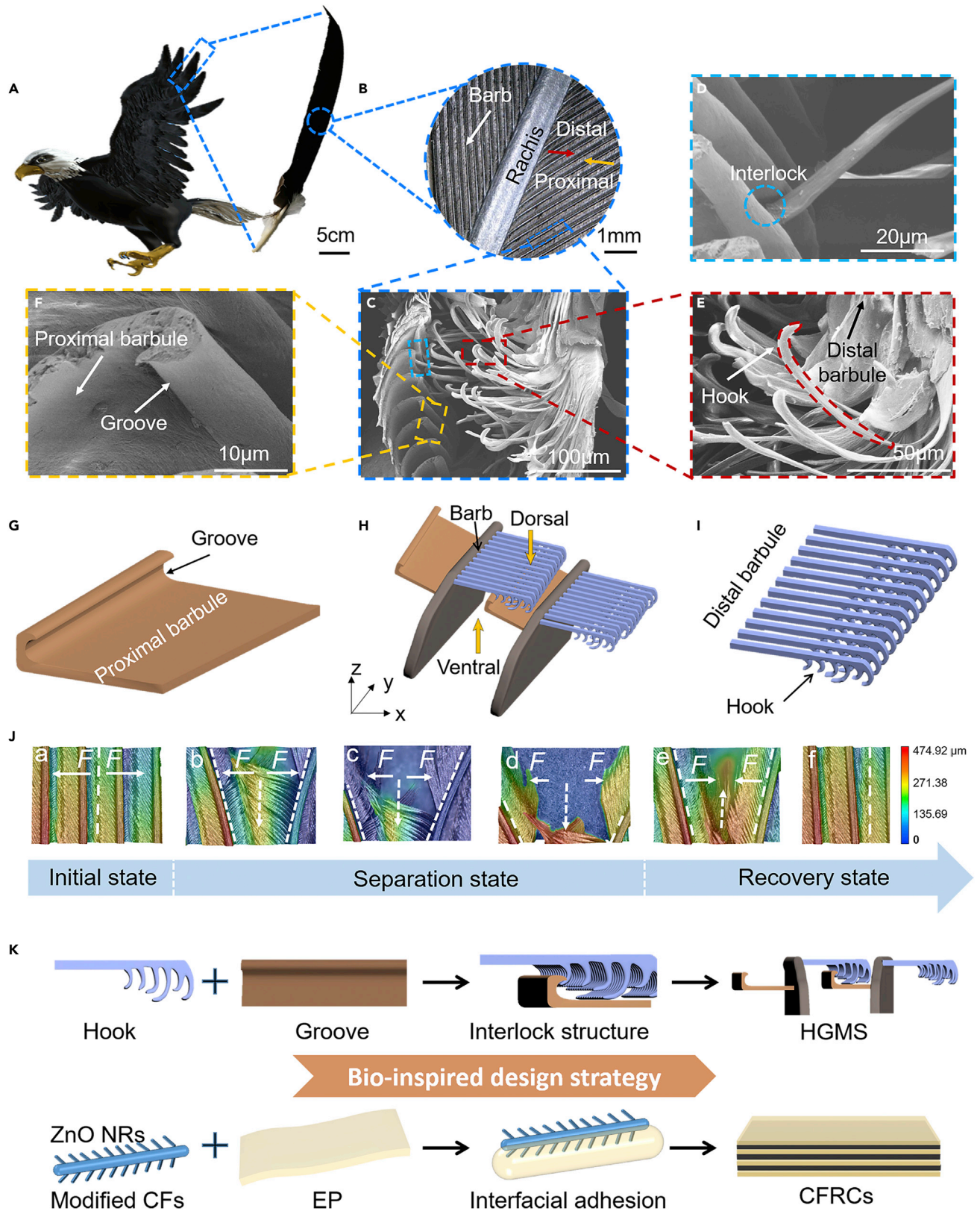
Figure content labeled A–K with panels showing eagle feather structure and bio-inspired design.

A — 5cm

B — Barb, Rachis, Distal, Proximal — 1mm

D — Interlock — 20μm

F — Proximal barbule, Groove — 10μm

C — 100μm

E — Hook, Distal barbule — 50μm

G — Groove, Proximal barbule

H — Barb, Dorsal, Ventral — z, y, x

I — Distal barbule, Hook

J —
a F F — Initial state
b F F — Separation state
c F F
d F F
e F F
f
474.92 μm / 271.38 / 135.69 / 0
Initial state | Separation state | Recovery state

K —
Hook + Groove → Interlock structure → HGMS
Bio-inspired design strategy
ZnO NRs Modified CFs + EP → Interfacial adhesion → CFRCs

Figure 1. HGMS and mechanical interlocking mechanism in flight feather of Black Kite (*Milvus migrans*)
(A) A schematic of Black Kite (*Milvus migrans*) in flight.
(B) Rachis and vane (barbs and barbules) of a single wing feather. Red and yellow arrows indicate the distal region and proximal region, respectively.
(C) Interlocking structure between microscale hook and groove. Hook and groove are on the distal and proximal side of the barb barbules respectively. Barbules from neighboring barbs interlock with each other.
(D) Mechanical interlocking structure consists of hook and groove.
(E and F) Microscale hook structures and single groove structure.
(G–I) Model of adjacent barbs, hook structures, and single groove.
(J) Process of the adjacent barbs separated and viewed from the ventral side.
(K) Proposed bioinspired design strategy to enhance interlayer interfacial adhesion of CFRCs, in which modified CFs with ZnO NRs and thermoset EP were selected to mimic "hook" and "groove", respectively.

group of 3D visible structure models of the natural HGMS were built up (Figures 1G–1I). The position relationship in stereoscopic space of two adjacent barbs with highly ordered barbules was identified (Figure 1G). Here, these barbules can be divided into two types by their unique morphology, namely, regularly independent hook with cambered end (Figure 1H) and monolithic groove with curly edge (Figure 1I). It indicated that two adjacent barbs are actually parallel with a naturally optimized distance, which makes it possible for neighboring barbules to interlock with each other. Thus, the natural HGMS in barbs is able to hold neighboring feathers together tightly to form compact feather vanes. More importantly, the natural HGMS significantly enhanced mechanical performance of feather vanes by novel interlocking mechanism to effectively tickle complex external load.

To experimentally reveal the underlying work mechanism of the natural HGMS for interfacial mechanical enhancement of feather vanes, an intuitive tear resistance test of the natural HGMS was performed (Video S1 Separation process of adjacent barbs viewed from ventral side. Related to Figure 1 and Video S2 Separation process of adjacent barbs viewed from dorsal side. Related to Figure 1). According to the connection status, the work process of the natural HGMS can be divided into six different connection states (Figures 1J and S1G). For the initial state, barbs are arranged in order and connected with each other tightly, presenting a compact feather vane (Figures 1Ja and S1Ga). When external force (*F*) in opposite directions was applied on two selected adjacent barbs, the natural HGMS started to demonstrate mechanical resistance to separation (Figures 1Jb and S1Gb). With *F* increasing, the adjacent barbs were gradually separated through unhooking connection between hook and groove. Meanwhile, the gap between the adjacent barbs was prolonged along the connecting line (Figures 1Jc and S1Gc). Then, the adjacent barbs were separated totally with the complete unhooking of the whole natural HGMS (Figures 1Jd and S1Gd). Surprisingly, when *F* was orientationally applied along the axial direction of the separated barbs, the microscale hooks and grooves can reconnect with each other smoothly (Figures 1Je and S1Ge). Finally, when the gap between adjacent barbs closed, the natural HGMS recovered to the initial state (Figures 1Jf and S1Gf).

Besides, composition characterization and analysis of the natural HGMS from original feather vanes was carefully performed by energy dispersive spectroscopy (EDS) and Fourier-transform infrared spectroscopy (FTIR). As a typical cuticularized derivant of epidermal cells of birds, feather vanes with the natural HGMS were inferred to mainly consist of organic matter. As expected, general chemical elements including C (57.10 wt %), O (21.76 wt %), N (14.86 wt %), and S (4.66 wt %) from organic compounds and thimbleful metal element Ca (0.93 wt %) were identified quantitatively (Figure S1E). Further, the existence of functional groups like -SH, -CH_2-, -NH_2, and -COOH from cystine ($C_3H_7NO_2S$) in keratin, the major protein of original feather vanes, were confirmed (Priemel et al., 2021; Lichtenegger et al., 2002). It indirectly validated that both the simple chemical composition and the delicate HGMS dominated the excellent mechanical performance of feather vanes (Figure S1F).

To fully take advantage of the unique HGMS, a bioinspired design strategy based on the mechanical interlocking mechanism was proposed to enhance interlayer interfacial adhesion of CFRCs (Figure 1K). Here, to realize the similarity on both morphology and function, modified CFs with ZnO nanorods (NRs) and thermoset EP were selected to mimic "hook" and "groove," respectively, which was anticipated to enhance the interfacial strength between CFs and EP. It was hypothesized that the ZnO NRs with rich superficial area can significantly increase the contact area with EP to realize interfacial adhesion enhancement via interlocking effect between CFs and EP. Finally, the CFRCs were laminated using the modified CFs with EP. Through the proposed bioinspired design strategy, CFRCs with high mechanical performance were expected to be obtained.
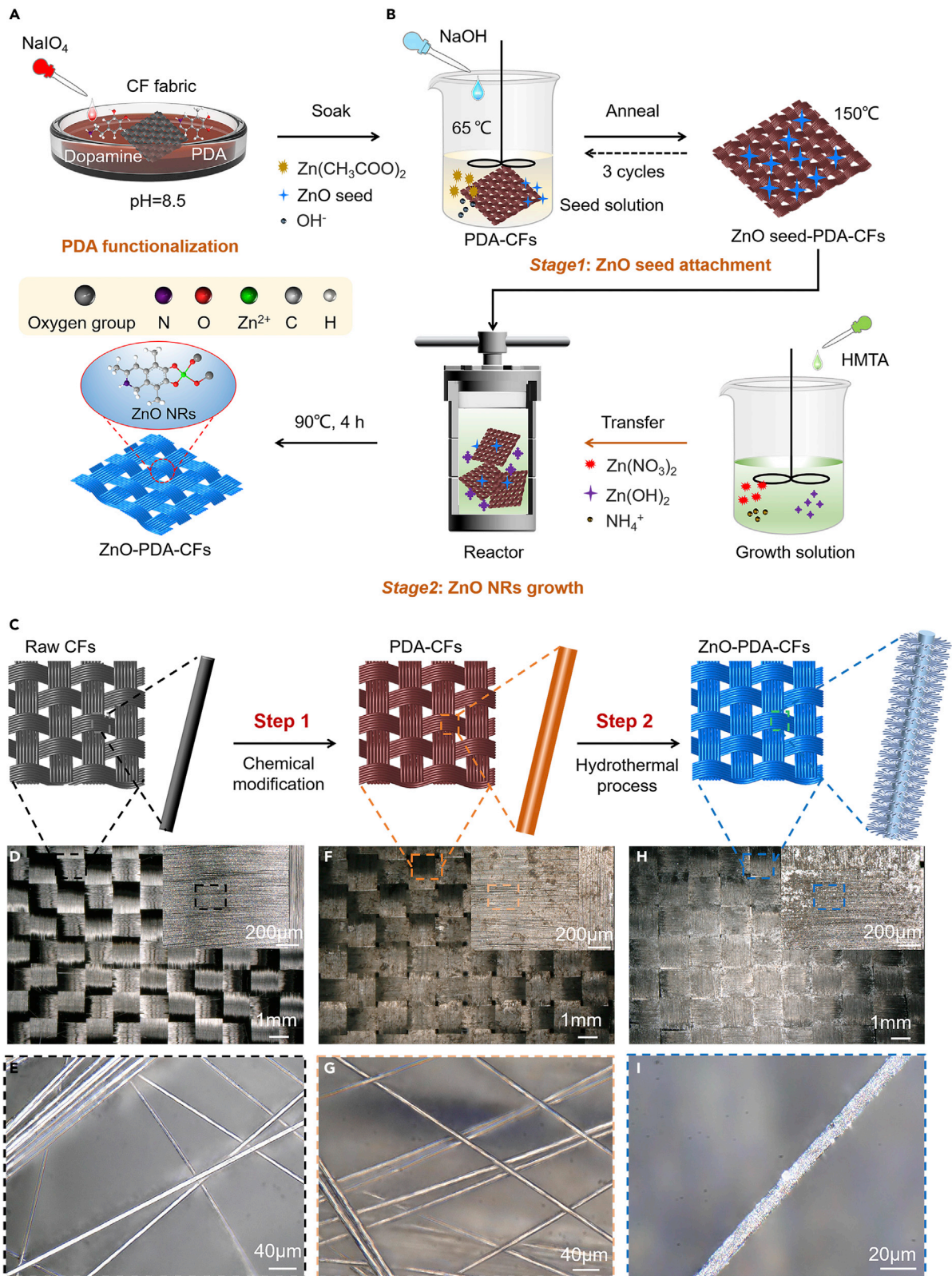
A

NaIO₄

CF fabric

Dopamine   PDA

pH=8.5

PDA functionalization

| Oxygen group | N | O | Zn²⁺ | C | H |

ZnO NRs

90°C, 4 h

ZnO-PDA-CFs

B

NaOH

65 °C

★ Zn(CH₃COO)₂
✚ ZnO seed
• OH⁻

PDA-CFs

Anneal

3 cycles

Seed solution

150°C

ZnO seed-PDA-CFs

Stage1: ZnO seed attachment

Reactor

Transfer

※ Zn(NO₃)₂
✚ Zn(OH)₂
• NH₄⁺

HMTA

Growth solution

Stage2: ZnO NRs growth

C

Raw CFs

Step 1
Chemical modification

PDA-CFs

Step 2
Hydrothermal process

ZnO-PDA-CFs

D

200μm

1mm

F

200μm

1mm

H

200μm

1mm

E

40μm

G

40μm

I

20μm

Figure 2. Schematics of the proposed two-step modification method and surface morphologies of the obtained modified CFs including PDA-CFs and ZnO-PDA-CFs

(A) PDA functionalization process. $NaIO_4$ accelerated the deposition of PDA at pH = 8.5.

(B) ZnO NRs growth via hydrothermal method. The whole process was divided into Zn^{2+} attachment on the surface of PDA-CFs in seed solution and ZnO NRs growth in hydrothermal synthesis reactor.

(C) Process diagram of chemical modification based on raw CFs. The surface of the raw CFs was functionalized by PDA and ZnO NRs were prepared by hydrothermal method to increase the surface roughness of the fibers.

(D–I) Optical images of raw CFs, PDA-CFs, and ZnO-PDA-CFs at different magnifications. The surface color of raw CFs changed from bright to brown after PDA modification and crystallization can be found on fiber surface after ZnO NRs growth.

Preparation, characterization, and analysis of biomimetic HGMS

In terms of morphological and functional similarities of natural HGMS and biomimetic HGMS for interfacial adhesion, raw CFs from a commercial carbon fabric were firstly obtained to construct the hook-like structure by a mild two-step modified method including modification of raw CFs with polydopamine (PDA) (Figure 2A) and ZnO-PDA-CFs preparation using hydrothermal method (Figure 2B). PDA can be easily deposited on most surfaces in a mild aqueous solution and is widely used as a green surface modifier. For the first functionalization of raw CFs, dopamine was oxidized by sodium periodate ($NaIO_4$) at pH = 8.5. Then, a self-polymerized thin layer with deposited PDA nanoparticles (NPs) was coated on raw CFs to form PDA-CFs. It was found that it generally takes 24 h for the dopamine solution to change from light brown to black after the polymerization, whereas the dopamine solution with the addition of $NaIO_4$ instantly changes to deep red instantly to complete the polymerization (Figure S2). It indicated that sodium periodate as a strong oxidant significantly shortened the time of dopamine self-polymerization and accelerated the deposition of PDA NPs on the surface of raw CFs. For the second functionalization based on PDA-CFs, ZnO NRs were grown on fiber surface via hydrothermal method (Figure 2B). This step aimed to morphologically and functionally mimic the natural HGMS to further realize the enhancement of interfacial adhesion between CFs and EP. It should be noted that two stages were involved in this step, namely ZnO seed attachment and ZnO NRs growth. For ZnO seed attachment, PDA-CFs were firstly soaked into ZnO seed solution (65 °C, NaOH, $Zn(CH_3COO)_2 \cdot 2H_2O$ and EtOH mixture). then annealed 10 min at 150 °C for 3 times. For ZnO NRs growth, ZnO NRs grew on the seed attachment sites on the surface of the obtained PDA-CFs in growth solution ($Zn(NO3)_2 \cdot 6H_2O$ and hexamethylenetetramine (HMTA) mixture) at 90 °C for 4 h. During the whole step, zinc ions (Zn^{2+}) formed coordination bonds with oxygen-containing functional groups; finally, ZnO NRs were obtained to form ZnO-PDA-CFs. The two-step modification process was also summarized through simplified schematics for a better understanding of the preliminary construction of biomimetic HGMS (Figure 2C).

Simultaneously, the surface morphology of carbon fabric and individual CF with different treatments was fully characterized by using a stereoscopic microscope under different magnifications (Figures 2D–2I and S3A–S3C). The surface of raw carbon fabric manufactured by plain wave technique was black and shiny (Figures 2D, 2E and S3A), whereas the surface of PDA-CFs was a bit brown (Figures 2F, 2G and S3B). There were some white grains on the surface of ZnO-PDA-CFs (Figures 2H, 2I and S3C), which were synthesized and later grew during the abovementioned hydrothermal process. To further evaluate the surface modification of CFs, surface morphology and chemical composite of individual CF were characterized using scanning electron microscopy (SEM) in detail.

The surface morphology of different CFs was well represented by the simplified models (Figures 3A, 3D and 3G). It was found that the surface of raw CFs was very clean with smooth microscale grooves along the longitudinal direction of the fiber (Figures 3B and 3C). Obviously, it is difficult for the original smooth surface to form strong mechanical locking with a resin matrix. In contrast, the surface of PDA-CFs was covered by a rough polymer film and the PDA NPs were uniformly deposited on the fiber surface (Figures 3E and 3F). Dense and uniform ZnO NRs were arranged vertically on the surface of ZnO-PDA-CFs (Figures 3H and 3I). In detail, the prepared ZnO NRs have good uniformity, which makes it possible to statistically analyze the diameter and length of ZnO NRs. The diameter and length of ZnO NRs in the randomly selected ZnO-PDA-CFs were measured at multiple locations (Figures S4A and S4B). The statistical results indicated the diameters of most the counted ZnO NRs to be 0.26–0.32 μm and the lengths were 1.1–1.5 μm (Figures S4C and S4D).

To further verify the successful growth of ZnO NRs on the PDA-CFs, chemical composition and element distribution on the surface of as-prepared ZnO-PDA-CFs were quantitatively and qualitatively characterized
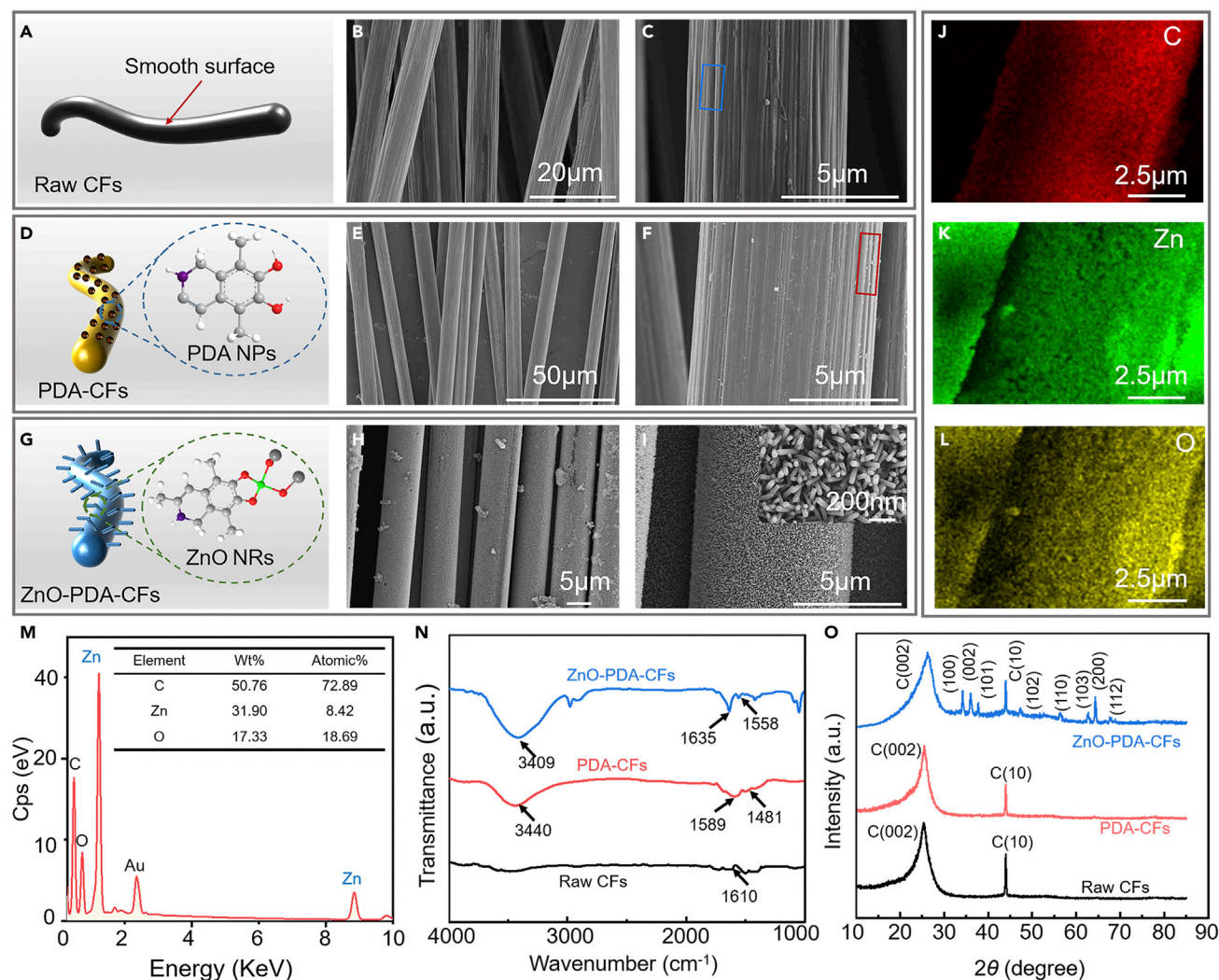
Figure 3. Morphological characteristics and chemical composite analysis of raw CFs, PDA-CFs, and ZnO-PDA-CFs

(A–C) Individual raw CF and SEM images of raw CFs under low and high magnifications, respectively. The raw CFs surface was clean and smooth microscale grooves can be seen (blue square).

(D–F) Individual PDA-functionalized CF and SEM images of PDA-CFs under low and high magnifications, respectively. Uniformly PDA NPs can be seen on the fiber surface (red square).

(G–I) Individual PDA-CF covered by ZnO NRs and SEM images of ZnO-PDA-CFs under low and high magnifications, respectively. Dense ZnO NRs were distributed orderly on the surface of PDA-CFs (inset in I).

(J–L) Main element distribution of the prepared ZnO-PDA-CFs. Zn and O distributed throughout the fiber surface evenly.

(M) Element proportion of C, Zn, and O from ZnO-PDA-CFs. The element proportion of C, Zn, and O was 50.76 wt %, 31.90 wt %, and 17.33 wt %.

(N) FTIR spectra of raw CFs, PDA-CFs, and ZnO-PDA-CFs demonstrating clear peak changes.

(O) XRD spectra of raw CFs, PDA-CFs, and ZnO-PDA-CFs for peak comparison. Typical diffraction peaks of hexagonal wurtzite structure of ZnO can be found in the ZnO-PDA-CFs.

by EDS (Figures 3J–3M). The main elements including carbon (C), zinc (Zn), and oxygen (O) were found to be distributed uniformly (Figures 3J–3L). The element proportion of C, Zn, and O was 50.76 wt %, 31.90 wt %, and 17.33 wt %, respectively (Figure 3M). It provided the preliminary evidence that dense ZnO NRs successfully grew on the surface of the PDA-CFs. Then, FTIR spectra of the three kinds of samples with premodification and post-modification were obtained (Figure 3N). For raw CFs, characteristic peak at 1610 cm^{-1} was found, which belonged to aromatic C-C stretching vibration. N-H shearing vibration peak appeared at 1480 cm^{-1}-1560 cm^{-1} in PDA-CFs and ZnO-PDA-CFs. The peak at 1589 cm^{-1} can be attributed to the stretching vibration of benzene ring in PDA-CFs, which moved to 1635 cm^{-1} after the growth of ZnO NRs. The shift of these peaks also indicated that the coordination between Zn^{2+} and

PDA took place. Both samples had a broad peak near 3400 cm^{-1}, which was caused by the stretching vibrations of functional groups like -NH$_2$, -NH-, and -OH in PDA. In addition, when compared to PDA-CFs, peak shifts can be found in ZnO-PDA-CFs. The reason could be that catechol groups in PDA as ligands coordinate with transition metal ion Zn^{2+} to form metal-ligand complexation, which can make ZnO seeds bond with PDA-CFs closely (Wang et al., 2018; Song et al., 2017). It also endowed ZnO NRs a good interfacial bond with PDA-CFs. In addition, XRD spectra (Figure 3O) showed that there were two peaks at 26 and 42° of the raw CFs and PDA-CFs, which belonged to C (002) and C (10). In contrast, many new diffraction peaks appeared in the ZnO-PDA-CFs, which were at 31.6° (100), 34.3° (002), 36.5° (101), 47.5° (102), 56.5° (110), 62.4° (103), 66.1° (200), and 68.5° (112). All these diffraction peaks were in line with the hexagonal wurtzite structure of ZnO. It indicated that the ZnO NRs were obtained on the surface of PDA-CFs as expected.

Laminate fabrication and mechanical performance of the bioinspired CFRCs

For CFRCs in the form of laminate, strong interface adhesion between reinforcement phase fibers and resin matrix is the key to realize the load transfer from the surface to the fibers, which determines the mechanical properties of the CFRCs. To verify the mechanical enhancement of the bioinspired CFRCs, the laminate samples were fabricated with raw CFs, PDA-CFs, and ZnO-PDA-CFs using a VACM method including uniform EP coating and vacuum molding (Figure 4A). For the laminate samples of bioinspired CFRCs, commercial CF fabrics were modified with the proposed two-step modification method. Then, each modified CF fabric was covered with EP evenly and placed layer by layer to obtain fiber preforms with specific layers. Subsequently, a vacuum setup was applied to the fiber preforms to eliminate the remaining air bubbles and enhance interlaminar adhesion between adjacent CF fabrics (Figure S5). Finally, the laminate samples of bioinspired CFRCs were obtained successfully. Similarly, laminate samples of CFRCs with raw CFs and PDA-CFs were also fabricated for the following comparative study to evaluate their mechanical performance through standard tensile, bending, and interlamellar shear tests (Figures 4B, 4E, 4H and S7A–S7C). Further, to quantitatively describe the component proportion of above prepared CFRCs, content measurement of CF fabrics with raw CFs, PDA-CFs, and ZnO-PDA-CFs were conducted. According to the experimental result, it indicated the weights of CF fabrics (five pieces, 2.5 × 2.5 cm) with raw CFs, PDA-CFs, and ZnO-PDA-CFs were 710.6 ± 0.7 mg, 727.7 ± 1.2 mg, and 743.2 ± 1.6 mg, respectively. The weight increased gradually from CFs to PDA-CFs then to ZnO-PDA-CFs because of the addition of PDA (1.14 wt %) and ZnO NRs (1.05 wt %). Finally, the bioinspired CFRCs with five-layer ZnO-PDA-CFs were prepared to weigh. After simple calculation, the composition proportion of the prepared bioinspired CFRCs is as follows: CFs (47.96 wt %), EP (49.85 wt %), ZnO (1.14 wt %), and PDA (1.05 wt %) (Figure S6).

During mechanical tests, at least five groups of valid data were collected for each kind of laminate sample to calculate their strength values. To reflect every real test result, all the five curves of each kind of sample were plotted with the same color (Figures 4C, 4F, and 4I). Load-displacement curves of three groups of laminate samples were obtained under tensile test (Figure 4C). By a simple calculation, the tensile strengths of laminate samples prepared with raw CFs, PDA-CFs, and ZnO-PDA-CFs can reach up to about 562.25, 577.40, and 591.20 MPa, respectively (Figure 4D). Compared to the laminate samples with raw CFs, the tensile strength of the laminate samples with PDA-CFs and ZnO-PDA-CFs increased by 2.69 and 5.15%, respectively. In addition, the tensile modulus of the three groups of laminate samples also had little difference (about 34.18, 35.00 and 34.70 GPa). The reason could be that tensile strength of the laminate samples mainly depend on the axial fracture strength of the CFs rather than the interface strength between the fibers and the resin matrix. However, the flexural strength and modulus of laminate samples with raw CFs were about 396.43 MPa and 50.23 GPa, respectively (Figures 4F and 4G). After modification with PDA, the flexural strength and modulus of laminate samples with PDA-CFs increased to about 455.13 MPa and 52.66 GPa, respectively. Namely, the flexural strength and modulus of the modified laminate samples can increase by 14.81 and 4.84%, respectively. More surprisingly, the flexural strength and modulus of laminate samples with ZnO-PDA-CFs can reach to about 555.07 MPa and 72.54 GPa, respectively, which were 40.02 and 44.42% higher than that of laminate samples with raw CFs. It provided clear evidence that two-step modification was effective for the mechanical performance improvement of laminate CFRCs.

Further, to investigate the interface performance of the laminate CFRCs, interlaminar shear tests of three kinds of laminate samples were carried out. The interlaminar shear strength (ILSS) of laminate samples with raw CFs, PDA-CFs, and ZnO-PDA-CFs were about 18.97, 29.61, and 38.25 MPa, respectively (Figures 4I and 4J). Meanwhile, the corresponding modulus of these samples was also obtained with
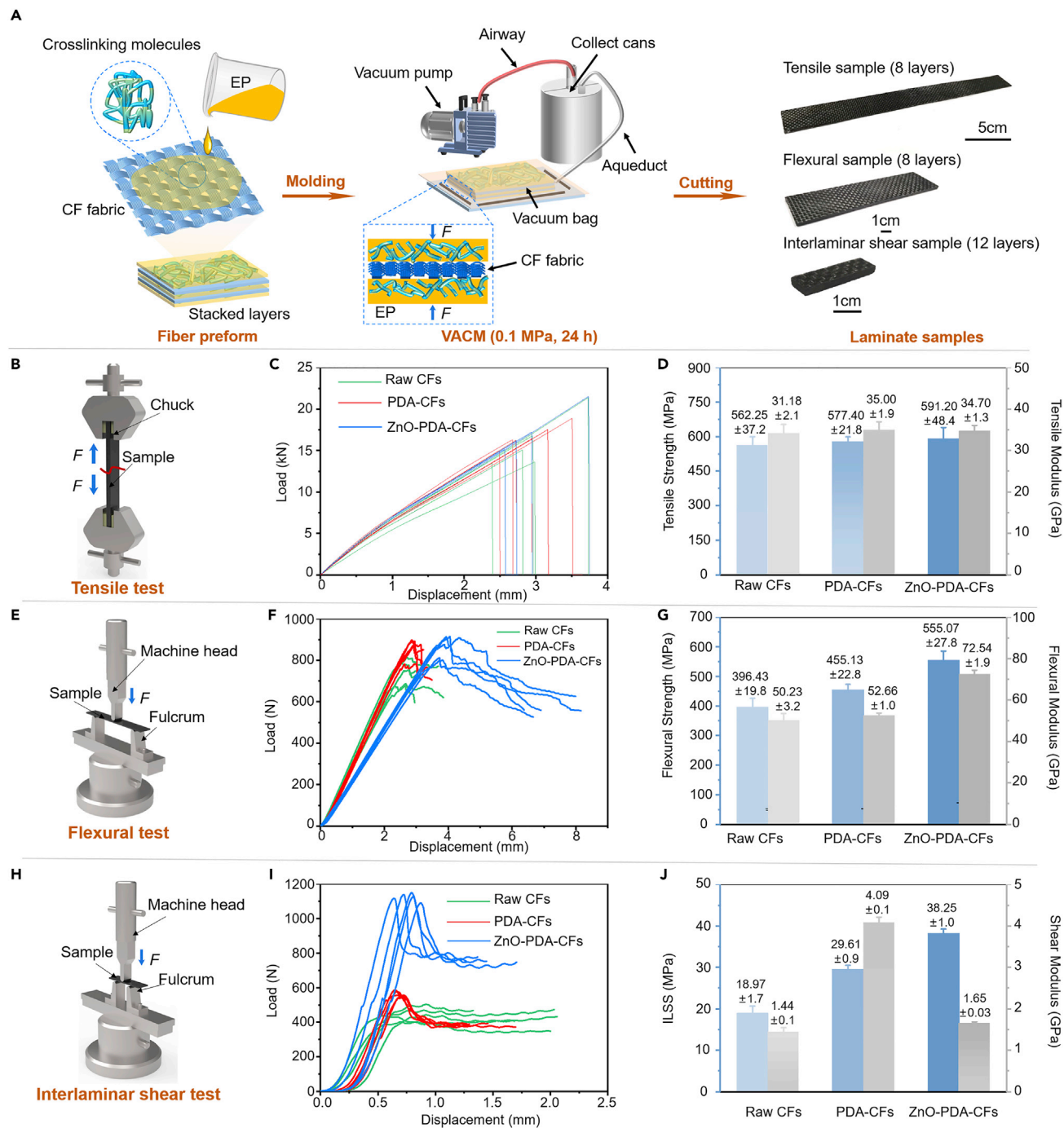
Figure 4. Fabrication process of laminate samples of CFRCs and three standard mechanical tests

Data are represented as (mean ± SE).

(A) Schematic of fabrication process of laminate samples for mechanical tests. Fabrication process of laminate samples can be divided into three steps: fiber preform achievement, VACM, and mechanical cutting for laminate samples with standard sizes.

(B–D) Tensile test setup, load-displacement curves, and tensile strength and modulus. The tensile strength and modulus of the three groups of laminate samples had little difference.

(E–G) Flexural test setup, load-displacement curves, and flexural strength and modulus. The flexural strength and modulus of laminate samples with ZnO-PDA-CFs were 40.02 and 44.42% higher than that of laminate samples with raw CFs.

(H–J) Interlaminar shear test setup, load-displacement curves, and ILSS and shear modulus. The ILSS and shear modulus of laminate samples with ZnO-PDA-CFs were 101.63 and 14.55% higher than that of laminate samples with raw CFs.
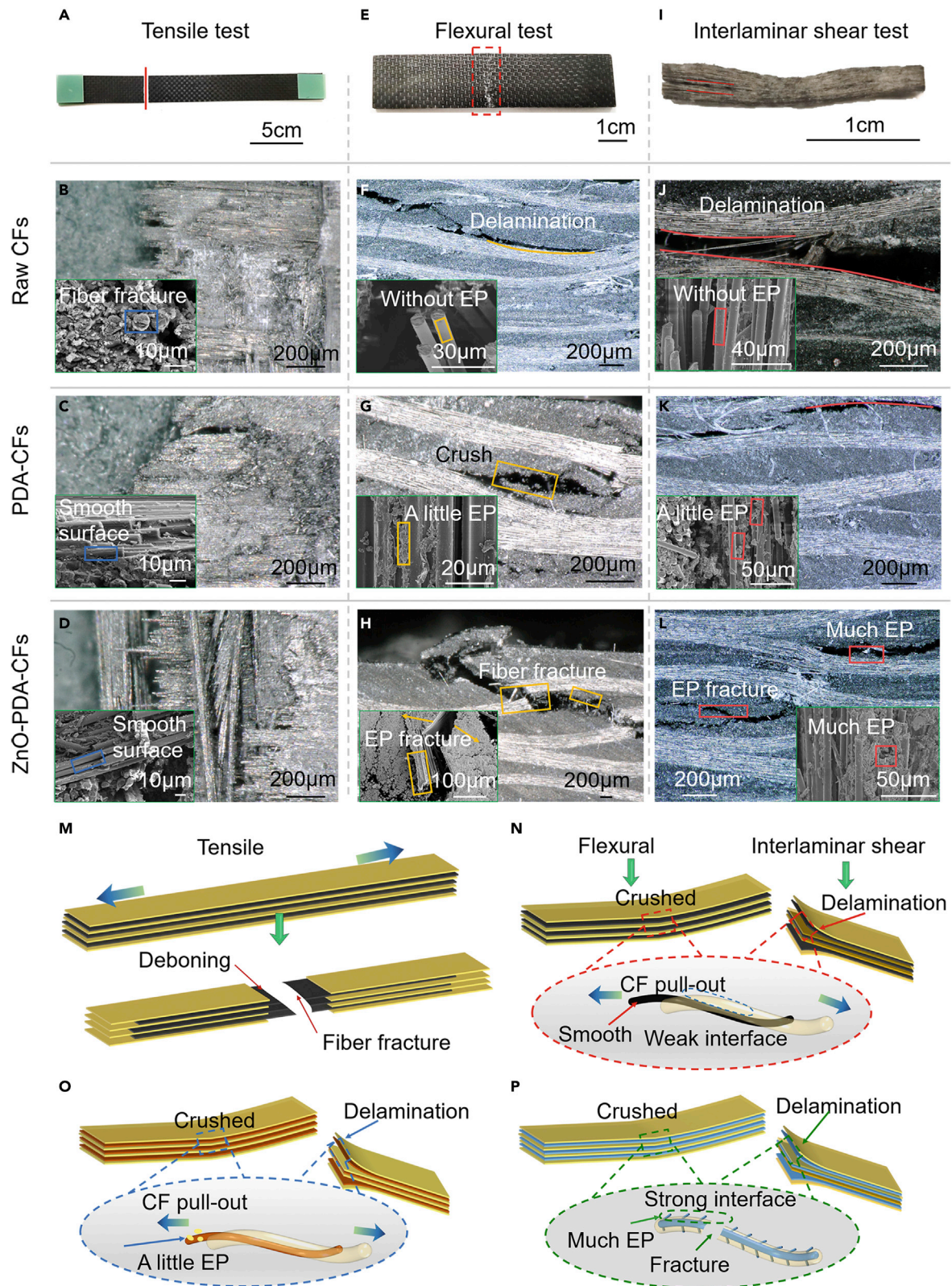
A — Tensile test — 5cm

E — Flexural test — 1cm

I — Interlaminar shear test — 1cm

Raw CFs

B — Fiber fracture — 10μm — 200μm

F — Delamination — Without EP — 30μm — 200μm

J — Delamination — Without EP — 40μm — 200μm

PDA-CFs

C — Smooth surface — 10μm — 200μm

G — Crush — A little EP — 20μm — 200μm

K — A little EP — 50μm — 200μm

ZnO-PDA-CFs

D — Smooth surface — 10μm — 200μm

H — Fiber fracture — EP fracture — 100μm — 200μm

L — Much EP — EP fracture — Much EP — 200μm — 50μm

M — Tensile — Deboning — Fiber fracture

N — Flexural — Crushed — Interlaminar shear — Delamination — CF pull-out — Smooth — Weak interface

O — Crushed — Delamination — CF pull-out — A little EP

P — Crushed — Delamination — Strong interface — Much EP — Fracture

Figure 5. Failure modes after tensile, flexural, and interlaminar shear tests and mechanical enhancement analysis

(A, E, and I) Failure modes and positions after tensile, flexural, and interlaminar shear tests. Fractured zone in tensile failure was along the width (red line) and appeared in the middle of the laminate samples. Laminate samples with flexural failure were crushed in the stress point area (red dashed box) and an obvious crease can be found there. Distinct delamination occurred at the end of the failure pattern for the laminate samples suffering from interlaminar shear failure.

(B–D) Microscale morphologies of fractured surfaces of laminate samples with raw CFs, PDA-CFs, and ZnO-PDA-CFs after tensile test. The surface of pull-out fibers was smooth and there was almost no epoxy remaining.

(F–H) Microscale morphologies of fractured surfaces of laminate samples with raw CFs, PDA-CFs, and ZnO-PDA-CFs after flexural test.

(J–L) Microscale morphologies of fractured surfaces of laminate samples with raw CFs, PDA-CFs, and ZnO-PDA-CFs after interlaminar shear tests. The microscale morphologies of fractured surfaces here were very similar with that after flexural tests.

(M) Failure mode of laminate samples after tensile test. The whole failure process can be divided into fiber-resin debonding and fiber axial fracture.

(N–P) Mechanical enhancement mechanism of laminate samples with raw CFs, PDA-CFs, and ZnO-PDA-CFs during flexural and interlaminar shear tests.

the values of about 1.44, 4.09, and 1.65 GPa. Compared to original laminate samples, the ILSS and modulus of the laminate samples with ZnO-PDA-CFs increased by 101.63 and 14.55%, respectively. In this case, it can be concluded that the ILSS of the laminate CFRCs can be significantly improved by the bioinspired design strategy through morphologically and functionally mimicking the natural HGMS. On the one hand, it benefited from the intrinsic strong interface between reinforcement phase fibers and resin matrix. On the other hand, the presence of ZnO NRs enhanced the mechanical connection between adjacent fabric layers.

Comparative analysis of mechanical enhancement mechanism

After abovementioned tensile, flexural, and interlaminar shearing tests, failure morphologies of these laminate CFRCs were experimentally characterized. By comparative analysis of the failure modes of each sample, the underlying mechanism of mechanical enhancement performance of the biinspired CFRCs was revealed deeply. Firstly, the macroscopic failure modes and positions of these laminate CFRCs after mechanical tests were observed directly. For the tensile test, laminate samples fractured in the middle (Figure 5A), whereas for flexural test, samples were crushed in the stress point (Figure 5E). For interlaminar shear test, distinct delamination occurred at the end of the pattern (Figure 5I). The microscale morphologies and more details of the fracture surface of laminate samples after mechanical tests were characterized. It was found that the main failure modes of these samples were fiber fracture. It showed that the surface of the pull-out fibers was smooth and there almost no epoxy remained after tensile tests (Figures 5B–5D and S8A–S8C). It proved that the tensile strength of the samples mainly depended on the axial fracture strength of the fibers rather than the interface strength between the reinforcement phase fibers and resin matrix. However, tensile tests did not verify the significant advantage of the bioinspired design for interfacial mechanical enhancement. The reason could be that the axial fracture strength of fiber was much higher than the interface strength between fibers and resin.

In contrast, the failure mode and microscale morphologies of fractured surfaces of these laminate samples after flexural and interlaminar shear tests were also investigated. For laminate samples with raw CFs, abundant fibers were pulled out from the resin matrix and the fracture surface was almost smooth without epoxy remaining on the surface of pull-out CFs (inset in Figure 5F). However, for laminate samples with PDA-CFs, a small amount of fibers were pulled out from the resin matrix with a little residue epoxy remaining on the surface of the exposed PDA-CFs (inset in Figure 5G). Interestingly, there were nearly no scattered fibers and a large amount of epoxy remained on the surface of ZnO-PDA-CFs. It was found that the failure mode of laminate samples with raw CFs after flexural test was mainly delamination caused by debonding between CFs and epoxy. There were many fibers pulled out from the epoxy and the fracture surface was almost smooth without resin remaining (Figures 5F, 5J, S8D, and S8G). It indicated that the interface between raw CFs and epoxy was relatively weak. Even if the laminate sample was damaged, the intrinsic excellent mechanical properties of raw CFs were not fully performed. For laminate samples with PDA-CFs after flexural and interlaminar shear tests, it can be observed from the fracture surface that the failure was also mainly caused by debonding between the CFs and resin. However, a small amount of CFs was pulled out from the resin matrix with a little residue resin on the surface of the exposed CFs (Figures 5G, 5K, S8E, and S8H). The reason could be that the PDA coating on the fiber surface introduced a large number of reactive oxygen, which improved the surface activity of the CFs and enhanced molecular bonding between the PDA-CFs and resin. As a result, the interfacial adhesion was significantly improved. However, the enhancement of interfacial strength was limited because of the weak mechanical connection between the smooth PDA-CFs and resin. In contrast, for laminate samples with ZnO-PDA-CFs, ZnO NRs on the fiber surface can provide better wettability and mechanical connection with the resin, which significantly increases the contact area

between every individual fiber and resin. At the same time, the nanoscal-reinforced interface can effectively enhance the stress transfer and alleviate stress concentration. Although part delamination was also caused by debonding between the CFs and resin, the pull-out degree of the fibers was significantly reduced and the main failure form was the fracture of the resin matrix. In addition, there were nearly no scattered fibers and a large amount of epoxy resin remained on the surface of ZnO-PDA-CFs (Figures 5H, 5L, S8F, and S8I). When the bioinspired CFRPs are loaded, the load can be transferred to the fibers through the strong interface between the ZnO-PDA-CFs and the resin matrix. It gives full play to the mechanical strength of the CFs. Interestingly, it is consistent with the work mechanism of natural HGMS that transfer load to barbs through strong interfacial interaction to ensure the strength of the whole feather vane.

According to the above results, the mechanical enhancement mechanism analysis toward different laminate samples after mechanical tests was summarized schematically (Figures 5M–5P). For tensile test, the tensile strength of the laminate samples did not depend on the interface strength between the CFs and the resin matrix but the axial fracture strength of the CFs. When tensile samples were fractured, debonding between CFs and EP occurred firstly then internal CFs fractured (Figure 5M). For flexural and interlaminar shear tests, because of the weak interface adhesion between CFs and EP, the main failure mode was delamination caused by debonding between raw CFs and EP (Figure 5N). When the weak interface was damaged by external load, the load cannot be transferred to the CFs effectively. At this time, the laminate samples were structurally destroyed but the applied load was far less than the ideally required limit load for the fibers or resin. In contrast, the PDA coating on the CFs introduced a large amount of reactive oxygen-containing functional groups, so the interfacial adhesion was improved to some extent. When the external load was applied to reach the fracture threshold, the stronger interface failure occurred with a little resin remaining (Figure 5O). Although the tolerance load value at this time was higher, there was still a lack of an effective mechanical connection between CFs and EP, which resulted in unstable interface strength. In comparison, for the bioinspired laminate samples with ZnO-PDA-CFs, the fracture of resin and fibers became the main failure modes. There was much resin on CFs when the resin fractured (Figure 5P).

It can be inferred that fiber modification contributed to the improved mechanical performance of the laminate samples. Before modification, the laminate samples were delaminated because of the debonding between fibers and resin and there was almost no resin residue on the surface of the pull-out fibers. At this time, the stress transfer ended at the weak interface. After modification, fibers or resin fracture occurred in the modified laminate samples and a large amount of resin remained on the fiber surface. This was because ZnO NRs enhanced the bonding strength between fiber and resin. When the laminates were loaded, the stress was successfully transferred to the fiber through the strong interface. Briefly, the original weak interface could lead to debonding failure between raw CFs and resin matrix, wheereas PDA-CFs can enhance the interface strength to a certain degree. It was experimentally confirmed that nanostructured ZnO as an interphase can endow fiber-matrix interface with improved mechanical performance through a combination of mechanical interlocking and increased surface area (Nasser et al., 2020). Thus, it can be reasonably inferred that the as-prepared ZnO-PDA-CFs with branching ZnO NRs can significantly increase the contact area in the interface zone and improve resin wettability of the fibers. The two factors work together to enhance the interfacial connection between the CFs and resin matrix thus improving the global mechanical performance of the laminate samples.

Further, the active groups on the surface of the modified CFs and the epoxy groups in the resin could be closely cross-linked through chemical bonds to provide stronger interfacial strength (Patterson et al., 2015). To confirm the modification validity of ZnO NRs, a qualitative test of interface strength between CFs and resin was performed (Figure S9A). The load-displacement curves of three different fibers were obtained for strength comparison (Figure S9B). When compared to raw CFs and PDA-CFs, ZnO-PDA-CFs demonstrated the strongest bond strength with a peak load of 22.52 ± 3.15 N (Figure S9C). The peak load of ZnO-PDA-CFs increased by 98.94 and 41.28% than that of raw CFs (11.32 ± 1.39 N) and PDA-CFs (15.94 ± 1.07 N), respectively, which also provided additional evidence for the effectiveness of surface modification with ZnO NRs. Moreover, a resin infiltration capacity (RIC) test was also conducted to compare fiber surface wettability (Figure S10A). The final RIC of raw CFs was 11.64 ± 1.10 mg, whereas the RIC of PDA-CFs increased by 24.57% and reached 14.50 ± 0.52 mg. Similarly, when compared to PDA-CFs, the RIC of ZnO-PDA-CFs was 17.54 ± 0.38 mg, which increased by 20.97% (Figures S10B and S10C). The results indicated that the ZnO-PDA-CFs demonstrated much better epoxy wettability than both raw CFs and PDA-CFs. Thus, it can be concluded that ZnO NRs improved the epoxy wettability properties of the CFs thus

increased the mechanical connection between the CFs and resin, which allowed the ultimate laminate samples to bear a higher load until be destroyed.

DISCUSSION

In this study, the underlying microscale mechanical interlocking mechanism of natural HGMS in flight feathers of Black Kite (*M. migrans*) was experimentally revealed. By a two-step modification method, the surface of raw CFs was firstly functionalized by dopamine. Then, biomimetic HGMS was successfully constructed with ZnO NRs grown on the surface of PDA-CFs by hydrothermal method to improve the interfacial adhesion between the reinforced phase CFs and resin matrix. To investigate the influence of fiber modification on mechanical properties of the CFRCs, three kinds of laminate samples were fabricated by a VACM method including uniform EP coating and vacuum molding. The tensile strength, flexural strength, and interlaminar shear strength of the different laminate samples were experimentally tested and compared. The results showed that the flexural strength and ILSS of the bioinspired CFRCs increased by 40.02 and 101.63%, respectively. By comparing the fracture morphologies of the laminate samples, the interface adhesion between the reinforced phase CFs and resin matrix was proved to be enhanced after modification. The two-step modification method proposed in this work can effectively improve the interfacial adhesion between reinforced phase CFs and resin matrix and enhance mechanical properties of original CFRCs. Compared to many other conventional modification methods, such as coating, surface oxidation, nanofiller, or grafting, the mechanical enhancement effect as well as other foreseeable advantages of the proposed two-step modification method is considerable (Figure S11 and Table S1). It was anticipated to provide a facile way for biomimetic fabrication of laminate CFRCs with superior mechanical properties to promote the application of bioinspired composites in broad engineering fields.

Limitations of the study

Functional enhancement against morphological similarity between natural structures and biomimetic structures was traded off, so the hook characteristic was not reflected very well in the ZnO-PDA-CFs. Systematic mechanics modeling was a considerable option for failure analysis, which could further enhance the theoretical depth of this work. High mechanical performance bioinspired CFRCs in this work were fabricated under limited laboratory conditions; however,the molding of its large-scale structural components toward engineering application still needs to be further investigated.

STAR★METHODS

Detailed methods are provided in the online version of this paper and include the following:

- KEY RESOURCES TABLE
- RESOURCE AVAILABILITY
  - Lead contact
  - Materials availability
  - Data and code availability
- METHODS DETAILS
  - Materials
  - PDA-CFs preparation
  - ZnO-PDA-CFs preparation
  - Fabrication of bio-inspired laminate samples
  - Characterization of original wing feather and modified CFs
  - Content measurement of PDA, ZnO, EP and CFs in CFRCs
  - Mechanical test of bio-inspired CFRCs
  - Qualitative test of interface strength
  - Fiber surface wettability test

SUPPLEMENTAL INFORMATION

Supplemental information can be found online at https://doi.org/10.1016/j.isci.2022.104066.

ACKNOWLEDGMENTS

AUTHOR CONTRIBUTIONS

Y.W., Z.M. and Z.H. conceived the idea and designed the research plan. Y.W., Z.M. (Zhengzhi Mu) and Z.Z. conducted the morphological characterization of original feathers. Y.W. and W.S. conducted the surface modification of CFs. Y.W., Z.Z. and W.S. performed the preparation of the bioinspired composite samples. Y.W., Z.M. (Zhengzhi Mu), Z.Z., W.S. and D.Z. analyzed the experimental data of mechanical tests. Y.W. and Z.M. (Zhengzhi Mu) proposed the hook-groove interlocking mechanism for enhanced interfacial adhesion. Y.W. and Z.M. (Zhengzhi Mu) prepared and organized the main figures. S.Z., H.H., Z.M. (Zhe Ma), L.H., Y.L., B.Z., Z.W., B.L., J.Z. and S.N. participated in discussions of the experimental results. Y.W. and Z.M. (Zhengzhi Mu) wrote the manuscript with input from all cauthors. Z.M. (Zhengzhi Mu), Z.H. and L.R. supervised the research.

DECLARATION OF INTERESTS

The authors declare no competing interests.

REFERENCES

Abidin, M.S.Z., Herceg, T., Greenhalgh, E.S., Shaffer, M., and Bismarck, A. (2019). Enhanced fracture toughness of hierarchical carbon nanotube reinforced carbon fibre epoxy composites with engineered matrix microstructure. Compos. Sci. Technol. *170*, 85–92.

Acar, V., Erden, S., Sarikanat, M., Seki, Y., Akbulut, H., and Seydibeyoglu, M.O. (2020). Graphene oxide modified carbon fiber prepregs: a mechanical comparison of the effects of oxidation methods. Express Polym. Lett. *14*, 1106–1115.

Andideh, M., and Esfandeh, M. (2016). Statistical optimization of treatment conditions for the electrochemical oxidation of PAN-based carbon fiber by response surface methodology: application to carbon fiber/epoxy composite. Compos. Sci. Technol. *134*, 132–143.

Banerjee, P., Kumar, S., and Bose, S. (2021). Thermoreversible bonds and graphene oxide additives enhance the flexural and interlaminar shear strength of self-healing epoxy/carbon fiber laminates. ACS Appl. Nano Mater. *4*, 6821–6831.

Beggs, K.M., Servinis, L., Gengenbach, T.R., Huson, M.G., Fox, B.L., and Henderson, L.C. (2015). A systematic study of carbon fibre surface grafting via in situ diazonium generation for improved interfacial shear strength in epoxy matrix composites. Compos. Sci. Technol. *118*, 31–38.

Chen, L., Du, Y.Z., Huang, Y.D., Ng, P.F., and Fei, B. (2016). Facile fabrication of hierarchically structured PBO-Ni(OH)(2)/NiOOH fibers for

enhancing interfacial strength in PBO fiber/epoxy resin composites. Compos. Sci. Technol. *129*, 86–92.

Cheng, Z., Han, Y.T., Luo, L.B., and Liu, X.Y. (2018a). Grafting degradable coordination polymer on aramid fiber surface to improve its interfacial properties. Mater. Lett. *233*, 102–106.

Cheng, Z., Zhang, L.J., Jiang, C., Dai, Y., Meng, C.B., Luo, L.B., and Liu, X.Y. (2018b). Aramid fiber with excellent interfacial properties suitable for resin composite in a wide polarity range. Chem. Eng. J. *347*, 483–492.

Chukov, D., Nematulloev, S., Torokhov, V., Stepashkin, A., Sherif, G., and Tcherdyntsev, V. (2019). Effect of carbon fiber surface modification on their interfacial interaction with polysulfone. Results. Phys. *15*, 102634.

Dai, Z.S., Zhang, B.Y., Shi, F.H., Li, M., Zhang, Z.G., and Gu, Y.Z. (2011). Effect of heat treatment on carbon fiber surface properties and fibers/epoxy interfacial adhesion. Appl. Surf. Sci. *257*, 8457–8461.

Eyckens, D.J., Demir, B., Randall, J.D., Gengenbach, T.R., Servinis, L., Walsh, T.R., and Henderson, L.C. (2020). Using molecular entanglement as a strategy to enhance carbon fiber-epoxy composite interfaces. Compos. Sci. Technol. *196*, 108225.

Fu, J.S., Zhang, M.J., Jin, L., Liu, L., Li, N., Shang, L., Li, M., Xiao, L.H., and Ao, Y.H. (2019). Enhancing interfacial properties of carbon fibers reinforced epoxy composites via layer-by-layer

self assembly GO/SiO$_2$ multilayers films on carbon fibers surface. Appl. Surf. Sci. *470*, 543–554.

Fu, Y.P., Li, H.X., and Cao, W.Y. (2020). Enhancing the interfacial properties of high-modulus carbon fiber reinforced polymer matrix composites via electrochemical surface oxidation and grafting. Compos. Part A. Appl. Sci. Manuf. *130*, 105719.

Garlof, S., Fukuda, T., Mecklenburg, M., Smazna, D., Mishra, Y.K., Adelung, R., Schulte, K., and Fiedler, B. (2016). Electro-mechanical piezoresistive properties of three dimensionally interconnected carbon aerogel (Aerographite)-epoxy composites. Compos. Sci. Technol. *134*, 226–233.

Garlof, S., Mecklenburg, M., Smazna, D., Mishra, Y.K., Adelung, R., Schulte, K., and Fiedler, B. (2017). 3D carbon networks and their polymer composites: fabrication and electromechanical investigations of neat Aerographite and Aerographite-based PNCs under compressive load. Carbon *111*, 103–112.

Han, Z.W., Mu, Z.Z., Li, B., Feng, X.M., Wang, Z., Zhang, J.Q., Niu, S.C., and Ren, L.Q. (2017). Bioinspired omnidirectional self-stable reflectors with multiscale hierarchical structures. ACS Appl. Mater. Inter. *9*, 29285–29294.

He, H.W., Zhang, T., and Yang, Y.K. (2021). A facile way to modify carbon fibers and its effect on mechanical properties of epoxy composites. J. Mater. Res. Technol. *10*, 164–174.

Hu, J.Q., Li, F., Wang, B., Zhang, H.Q., Ji, C.M., Wang, S.X., and Zhou, Z.G. (2020). A two-step combination strategy for significantly enhancing

the interfacial adhesion of CF/PPS composites: the liquid-phase oxidation followed by grafting of silane coupling agent. Compos. Part B Eng. *191*, 107966.

Huan, X.H., Shi, K., Yan, J.Q., Lin, S., Li, Y.J., Jia, X.L., and Yang, X.P. (2020). High performance epoxy composites prepared using recycled short carbon fiber with enhanced dispersibility and interfacial bonding through polydopamine surface-modification. Compos. Part B Eng. *193*, 107987.

Huang, W., Restrepo, D., Jung, J.Y., Su, F.Y., Liu, Z.Q., Ritchie, R.O., McKittrick, J., Zavattieri, P., and Kisailus, D. (2019). Multiscale toughening mechanisms in biological materials and bioinspired designs. Adv. Mater. *31*, 1901561.

Hung, P.Y., Lau, K.T., Fox, B., Hameed, N., Lee, J.H., and Hui, D. (2018). Surface modification of carbon fibre using graphene–related materials for multifunctional composites. Compos. Part B Eng. *133*, 240–257.

Hu, Z., Shao, Q., Huang, Y.D., Yu, L., Zhang, D.Y., Xu, X.R., Lin, J., Liu, H., and Guo, Z.H. (2018). Light triggered interfacial damage self-healing of poly (p-phenylene benzobisoxazole) fiber composites. Nanotechnology *29*, 185602.

Jia, C.Y., Yuan, C.C., Ma, Z.Y., Du, Y.Z., Liu, L., and Huang, Y.D. (2019). Improving the mechanical and surface properties of aramid fiber by grafting with 1,4-dichlorobutane under supercritical carbon dioxide. Materials *12*, 3766.

Jia, H., Liu, C., Qiao, Y., Zhang, Y., Dang, X.X., Chen, Y.S., and Jian, X.G. (2021). Enhanced interfacial and mechanical properties of basalt fiber reinforced poly (aryl ether nitrile ketone) composites by amino-silane coupling agents. Polymer *230*, 124028.

Jiao, Z.B., Chu, W.C., Liu, L.P., Mu, Z.Z., Li, B., Liao, Z.W., Wang, Y.C., Xue, H., Niu, S.C., Jiang, S.H., et al. (2020). Underwater writable and heat-insulated paper with robust fluorine-free superhydrophobic coatings. Nanoscale *12*, 8536–8545.

Karnati, S.R., Agbo, P., and Zhang, L.F. (2020). Applications of silica nanoparticles in glass/carbon fiber-reinforced epoxy nanocomposite. Compos. Commun. *17*, 32–41.

Kim, D.W., Wee, J.H., Yang, C.M., and Yang, K.S. (2020). Efficient removals of Hg and Cd in aqueous solution through NaOH-modified activated carbon fiber. Chem. Eng. J. *392*, 123768.

Kovalev, A., Filippov, A.E., and Gorb, S.N. (2014). Unzipping bird feathers. J. R. Soc. Interf. *11*, 20130988.

Krushnamurty, K., Rini, M., Srikanth, I., Ghosal, P., Das, A.P., Deepa, M., and Subrahmanyam, C. (2016). Conducting polymer coated graphene oxide reinforced C-epoxy composites for enhanced electrical conduction. Compos. Part A. Appl. Sci. Manuf. *80*, 237–243.

Kurtulus, C., Kuyumcu, M., Ciftci, M., and Tasdelen, M.A. (2021). Influence of POSS nanoparticles on the microstructure and mechanical properties of carbon fiber reinforced epoxy hybrid composites. Polym. Compos. *42*, 4056–4064.

Lau, K.T., Wong, T.T., Leng, J.S., Hui, D., and Rhee, K.Y. (2013). Property enhancement of polymer-based composites at cryogenic environment by using tailored carbon nanotubes. Compos. Part B Eng. *54*, 41–43.

Li, B., Luo, J.C., Huang, X.W., Lin, L.W., Wang, L., Hu, M.J., Tang, L.C., Xue, H.G., Gao, J.F., and Mai, Y.W. (2020a). A highly stretchable, super-hydrophobic strain sensor based on polydopamine and graphene reinforced nanofiber composite for human motion monitoring. Compos. Part B Eng. *181*, 107580.

Lichtenegger, H.C., Schoberl, T., Bartl, M.H., Waite, H., and Stucky, G.D. (2002). High abrasion resistance with sparse mineralization: copper biomineral in worm jaws. Science *298*, 389–392.

Li, F., Hua, Y., Qu, C.B., Xiao, H.M., and Fu, S.Y. (2016). Greatly enhanced cryogenic mechanical properties of short carbon fiber/polyethersulfone composites by graphene oxide coating. Compos. Part A. Appl. Sci. Manuf. *89*, 47–55.

Lin, J.W., Xu, P., Wang, L.L., Sun, Y.H., Ge, X., Li, G., and Yang, X.P. (2019). Multi-scale interphase construction of self-assembly naphthalenediimide/multi-wall carbon nanotube and enhanced interfacial properties of high-modulus carbon fiber composites. Compos. Sci. Technol. *184*, 107855.

Li, S.L., Zhang, C.Q., Fu, J.F., Zhou, Y.S., Sun, J.Q., He, Y., Nan, F., and Yu, Z.Z. (2020b). Interfacial modification of carbon fiber by carbon nanotube gas-phase dispersion. Compos. Sci. Technol. *195*, 108196.

Liu, H.S., Zhao, Y., Chen, F., Li, N., Sun, M.C., Zhang, T.Y., Sun, T.P., Wang, K., and Du, S.Y. (2021). Effects of polyetherimide sizing involving carbon nanotubes on interfacial performance of carbon fiber/polyetheretherketone composites. Polym. Adv. Technol. *32*, 3689–3700.

Liu, Z.D., Song, B., Wang, T.T., and Wang, L. (2020). Significant improved interfacial properties of PBO fibers composites by in-situ constructing rigid dendritic polymers on fiber surface. Appl. Surf. Sci. *512*, 145719.

Ma, L.C., Zhu, Y.Y., Feng, P.F., Song, G.J., Huang, Y.D., Liu, H., Zhang, J.X., Fan, J.C., Hou, H., and Guo, Z.H. (2019). Reinforcing carbon fiber epoxy composites with triazine derivatives functionalized graphene oxide modified sizing agent. Compos. Part B Eng. *176*, 107078.

McCoy, D.E., Feo, T., Harvey, T.A., and Prum, R.O. (2018). Structural absorption by barbule microstructures of super black bird of paradise feathers. Nat. Commun. *9*, 1.

Meyers, M.A., McKittrick, J., and Chen, P.Y. (2013). Structural biological materials: critical mechanics-materials connections. Science *339*, 773–779.

Mittal, G., Rhee, K.Y., Miskovic-Stankovic, V., and Hui, D. (2018). Reinforcements in multi-scale polymer composites: processing, properties, and applications. Compos. Part B Eng. *138*, 122–139.

Nasser, J., Lin, J.J., Steinke, K., and Sodano, H.A. (2019). Enhanced interfacial strength of aramid fiber reinforced composites through adsorbed aramid nanofiber coatings. Compos. Sci. Technol. *174*, 125–133.

Nasser, J., Steinke, K., Hwang, H.S., and Sodano, H. (2020). Nanostructured ZnO interphase for carbon fiber reinforced composites with strain rate tailored interfacial strength. Adv. Mater. Inter. *7*, 1901544.

Nie, C.X., Yang, Y., Cheng, C., Ma, L., Deng, J., Wang, L.R., and Zhao, C.S. (2017). Bioinspired and biocompatible carbon nanotube-Ag nanohybrid coatings for robust antibacterial applications. Acta Biomater. *51*, 479–494.

Niu, S.C., Li, B., Ye, J.F., Mu, Z.Z., Zhang, J.Q., Liu, Y., and Han, Z.W. (2016). Angle-dependent discoloration structures in wing scales of Morpho menelaus butterfly. Sci. China Technol. Sci. *59*, 749–755.

Patterson, B.A., Galan, U., and Sodano, H.A. (2015). Adhesive force measurement between HOPG and zinc oxide as an indicator for interfacial bonding of carbon fiber composites. ACS. Appl. Mater. Inter. *7*, 15380–15387.

Peng, J.S., and Cheng, Q.F. (2017). High-performance nanocomposites inspired by nature. Adv. Mater. *29*, 1702959.

Peng, J.S., Huang, C.J., Cao, C., Saiz, E., Du, Y., Dou, S.X., Tomsia, A.P., Wagner, H.D., Jiang, L., and Cheng, Q.F. (2020). Inverse nacre-like epoxy-graphene layered nanocomposites with integration of high toughness and self-monitoring. Matter *2*, 220–232.

Prakash, V.R.A., and Rajadurai, A. (2017). Inter laminar shear strength behavior of acid, base and silane treated E-glass fibre epoxy resin composites on drilling process. Def. Technol. *13*, 40–46.

Priemel, T., Palia, G., Forste, F., Jehle, F., Sviben, S., Mantouvalou, I., Zaslansky, P., Bertinetti, L., and Harrington, M.J. (2021). Microfluidic-like fabrication of metal ion-cured bioadhesives by mussels. Science *374*, 206–211.

Raphael, N., Namratha, K., Chandrashekar, B.N., Sadasivuni, K.K., Ponnamma, D., Smitha, A.S., Krishnaveni, S., Cheng, C., and Byrappa, K. (2018). Surface modification and grafting of carbon fibers: a route to better interface. Prog. Cryst. Growth CH. *64*, 75–101.

Samyn, P. (2020). Engineering the cellulose fiber interface in a polymer composite by mussel-inspired adhesive nanoparticles with intrinsic stress-sensitive responsivity. ACS Appl. Mater. Inter. *12*, 28819–28830.

Sepe, R., Bollino, F., Boccarusso, L., and Caputo, F. (2018). Influence of chemical treatments on mechanical properties of hemp fiber reinforced composites. Compos. Part B Eng. *133*, 210–217.

Sharma, M., Gao, S.L., Mader, E., Sharma, H., Wei, L.Y., and Bijwe, J. (2014). Carbon fiber surfaces and composite interphases. Compos. Sci. Technol. *102*, 35–50.

Song, P.A., Xu, Z.G., Dargusch, M.S., Chen, Z.G., Wang, H., and Guo, Q.P. (2017). Granular nanostructure: a facile biomimetic strategy for the design of super tough polymeric materials with high ductility and strength. Adv. Mater. *29*, 1704661.

Song, W.D., Mu, Z.Z., Zhang, Z.Y., Wang, Y.F., Hu, H.D., Ma, Z., Huang, L.W., Wang, Z., Zhang, B.J., Li, Y.J., et al. (2021). Cross-scale biological

models of species for future biomimetic composite design: a review. Coatings *11*, 1297.

Sun, Y., Yang, C.L., and Lu, Y.G. (2020). Weak layer exfoliation and an attempt for modification in anodic oxidation of PAN-based carbon fiber. J. Mater. Sci. *55*, 2372–2379.

Su, Y.A., Liu, P.P., Jing, D.Q., Zhang, X.H., and Zhang, S.C. (2021). Improved interfacial adhesion in carbon fiber/poly (ether ether ketone) composites with the sulfonated poly (ether ether ketone) sizing treatment. J. Appl. Polym. Sci. *138*, e51326.

Sullivan, T.N., Chon, M., Ramachandramoorthy, R., Roenbeck, M.R., Hung, T.T., Espinosa, H.D., and Meyers, M.A. (2017a). Reversible attachment with tailored permeability: the feather vane and bioinspired designs. Adv. Funct. Mater. *27*, 1702954.

Sullivan, T.N., Wang, B., Espinosa, H.D., and Meyers, M.A. (2017b). Extreme lightweight structures: avian feathers and bones. Mater. Today *20*, 377–391.

Wang, D., Bai, T., Cheng, W.L., Xu, C., Wang, G., Cheng, H.T., and Han, G.P. (2019). Surface modification of bamboo fibers to enhance the interfacial adhesion of epoxy resin-based composites prepared by resin transfer molding. Polymers *11*, 2107.

Wang, Z., Zhao, S.J., Kang, H.J., Zhang, W., Zhang, S.F., and Li, J.Z. (2018). Mussel byssus-inspired engineering of synergistic nanointerfacial interactions as sacrificial bonds into carbon nanotube-reinforced soy protein/ nanofibrillated cellulose nanocomposites: versatile mechanical enhancement. Appl. Surf. Sci. *434*, 1086–1100.

Wu, Q., Wan, Q.Q., Yang, X., Wang, F., Bai, H.H., and Zhu, J.F. (2021). Remarkably improved interfacial adhesion of pitch-based carbon fiber composites by constructing a synergistic hybrid network at interphase. Compos. Sci. Technol. *205*, 108648.

Wu, Z.J., Cui, H.Y., Chen, L., Jiang, D.W., Weng, L., Ma, Y.Y., Li, X.J., Zhang, X.H., Liu, H., Wang, N., et al. (2018). Interfacially reinforced unsaturated polyester carbon fiber composites with a vinyl ester-carbon nanotubes sizing agent. Compos. Sci. Technol. *164*, 195–203.

Yao, T.T., Zhang, X.F., Zhang, W.S., Liu, Y.T., Liu, Q.F., and Wu, G.P. (2021). Controlled attachment of polycarbonate nanoparticles on carbon fibers for increased resin impregnation and interfacial adhesion in carbon fiber composites. Compos. Part B Eng. *224*, 109218.

Zhan, J., Cao, X., Zhou, J.M., Xu, G., Lei, B., and Wu, M.H. (2021). Porous array with CoP nanoparticle modification derived from MOF grown on carbon cloth for effective alkaline hydrogen evolution. Chem. Eng. J. *416*, 128943.

Zhang, F.F., Zong, L.S., Weng, Z.H., Bao, F., Li, N., Wang, J.Y., and Jian, X.G. (2020a). Highly enhanced performance of epoxy composites via novel phthalazinone-bearing hybrid system as matrix. Compos. Part A. Appl. Sci. Manuf. *131*, 105772.

Zhang, F.L., Jiang, L., and Wang, S.T. (2018). Repairable cascaded slide-lock system endows bird feathers with tear-resistance and superdurability. Proc. Natl. Acad. Sci. U S A *115*, 10046–10051.

Zhang, M., Ding, L., Zheng, J., Liu, L.B., Alsulami, H., Kutbi, M.A., and Xu, J.L. (2020b). Surface modification of carbon fibers with hydrophilic Fe3O4 nanoparticles for nickel-based multifunctional composites. Appl. Surf. Sci. *509*, 145348.

Zhang, S.J., Zhang, J.Q., Zhu, B., Niu, S.C., Han, Z.W., and Ren, L.Q. (2020c). Progress in bio-inspired anti-solid particle erosion materials: learning from nature but going beyond nature. Chin. J. Mech. Eng. *33*, 42.

Zhao, Y.P., and Fan, X.Y. (2019). Feather evolution from knotted barbules to hooked and unhooked barbules and its finite element analysis. Micron *122*, 28–31.

Zhu, J.J., Yuan, L., Guan, Q.B., Liang, G.Z., and Gu, A.J. (2017). A novel strategy of fabricating high performance UV-resistant aramid fibers with simultaneously improved surface activity, thermal and mechanical properties through building polydopamine and graphene oxide bi-layer coatings. Chem. Eng. J. *310*, 134–147.

STAR★METHODS

KEY RESOURCES TABLE

REAGENT or RESOURCE	SOURCE	IDENTIFIER
Chemicals, peptides, and recombinant proteins		
Epoxy resin (E-51) AB adhesives	Kunshan Eituo Composites Co., Ltd., China	N/A
$Zn(CH_3COO)_2 \cdot 2H_2O$, 99.0%	Shanghai Aladdin Biochemical Technology Co., Ltd., China	CAS: 5970-45-6
Dopamine hydrochloride, 98.0%	Shanghai Aladdin Biochemical Technology Co., Ltd., China	CAS: 51-61-6
TRIS, 99.0%	Shanghai Aladdin Biochemical Technology Co., Ltd., China	CAS: 77-86-1
Sodium periodate	Shanghai Aladdin Biochemical Technology Co., Ltd., China	CAS: 7790-28-5
$Zn(NO_3)_2 \cdot 6H_2O$, 99.0%	Shanghai Aladdin Biochemical Technology Co., Ltd., China	CAS: 10198-18-6
HMTA, 99.0%	Shanghai Aladdin Biochemical Technology Co., Ltd., China	CAS: 100-97-0
Biological samples		
Feathers of Black Kite	Qiusheng Feather Workshop, China	https://m.tb.cn/h.fmqYLw0?tk=oK4s2f07bme
Other		
T300 CFs	Toray Ltd., Japan	N/A

RESOURCE AVAILABILITY

Lead contact

Further information and requests for resources and reagents should be directed to and will be fulfilled by the lead contact, Zhengzhi Mu (zmu@jlu.edu.cn).

Materials availability

This study did not generate new unique reagents.

Data and code availability

- All data reported in this paper will be shared by the lead contact upon request.
- This paper does not report original code.
- Any additional information required to reanalyze the data reported in this paper is available from the lead contact upon request.

METHODS DETAILS

Materials

The feathers were purchased from Qiusheng Feather Workshop (China) and only feathers rather than a vertebrate specimen were handled in this work. T300 CFs were purchased from Toray Ltd. (Japan). Surface sizing agent and contaminants of T300 CFs were removed by soaking in acetone for 72 h to obatin raw CFs. Epoxy resin (E-51) AB adhesives were supplied by Kunshan Eituo Composites Co., Ltd. (China). Acetone, zinc acetate dihydrate ($Zn(CH_3COO)_2 \cdot 2H_2O$, 99.0%), sodium hydroxide (NaOH, 96.0%), ethanol (99.7%), dopamine hydrochloride (98.0%), tris-(hydroxy-methyl) aminomethane (TRIS, 99.0%), sodium periodate (AR, $\geq$99.5%), zinc nitrate hexahydrate ($Zn(NO_3)_2 \cdot 6H_2O$, 99.0%) and hexamethylenetetramine (HMTA) ($C_6H_{12}N_4$, 99.0%) were purchased from Shanghai Aladdin Biochemical Technology Co., Ltd. (China) and used without further purification.

PDA-CFs preparation

T300 CFs were completely immersed in acetone for 72 h at room temperature to remove the sizing agent and pollutants on the surface, then raw CFs were obtained after cleaning and drying. Secondly, 1 g/L aqueous solution of dopamine hydrochloride was prepared with a stable pH = 8.5 by adding tris buffer. Thirdly, sodium periodate to dopamine hydrochloride with a molar ratio of 2:1 was added and stirred violently. Raw CFs were completely immersed in the solution for 6 h (Li et al., 2020b; Samyn., 2020; Song et al., 2017).

ZnO-PDA-CFs preparation

To prepare ZnO seed solution, 12.5 mmol/L zinc acetate ethanol solution (solution A) and 20 mmol/L sodium hydroxide ethanol solution (solution B) were stirred at 65°C for 30 min respectively. Then, the mixed solution (The volume ratio of solution A to solution B is 5:1) was continuously stirred for 30 min at 65°C and kept at room temperature for 1 h after it was cooled by ice water bath. PDA-CFs were completely immersed in the prepared ZnO seed solution for 15 min and the seed solution was stirred evenly to ensure the uniform seed synthesis. Afterwards, the soaked PDA-CFs were annealed in air atmosphere at 150°C for 10 min for three times. ZnO growth solution was prepared by adding 7.4373 g zinc nitrate hexahydrate and 3.5048 g HMTA to 500 mL deionized water. It was stirred evenly at room temperature for 30 min to fully dissolve. PDA-CFs was completely soaked in the growth solution at 90°C in a closed reactor for 4 h. Finally, they were cleaned by ultrasonic and placed in a vacuum drying oven at 100°C for 2 h to obtain ZnO-PDA-CFs.

Fabrication of bio-inspired laminate samples

Epoxy resin AB adhesive with the mass ratio of 3:1 was stirred evenly for 5 min to ensure the two components were mixed. Make sure that the worktable was dry and clean to spray the release agent. After the release agent was dried, carbon fiber fabrics were coated with epoxy resin and laid layer by layer. Then, the surface of the carbon fiber fabrics were covered with perforated isolation film, adhesive felt and vacuum bag film in turn. After sealing, the carbon fiber fabrics were vacuumized to a pressure of 0.1 MPa and cured at room temperature for more than 24 h. Finally, bio-inspired laminate samples were obtained.

Characterization of original wing feather and modified CFs

Feather samples were pretreated before characterization. They were soaked in anhydrous ethanol and ultrasonically treated (220 V, 40 Hz, 25°C) for 5 min to remove surface stains. After dried at 80°C for 2 h, a thin layer of Au NPs was coated on the surface of feather specimen using ion sputtering apparatus (Q150RS). With the help of a stereoscopic microscope (VHX-S650E) and SEM (JSM-6700F, JEOL), the morphologies and dimensions of the feathers and the fracture morphologies of bio-inspired composites were characterized under different magnifications. The element distribution maps of the modified CFs were obtained using an EDS (Oxford X-MaxN 150). FTIR (IRAffinity-1S-WL) was used to performed chemical analysis. The samples were mashed into powder and compressed into KBr (A.R.) flakes. In order to measure the crystal structure on the surface of raw CFs and modified CFs, XRD (Smartlab Sex-Ray generator 3 kW closed tube) with the range of 10°–80°(2θ) was used for measurement.

Content measurement of PDA, ZnO, EP and CFs in CFRCs

To evaluate the composition proportion of the prepared CFRCs, firstly, each single layer of fabrics with raw CFs, PDA-CFs and ZnO-PDA-CFs was respectively cut into pieces with the size of 2.5 cm × 2.5 cm. Then, every five pieces of above single layer was weighed to obtain their weight within specific area (2.5 cm × 2.5 cm).

Mechanical test of bio-inspired CFRCs

With the help of electrohydraulic universal testing machine (MTS 810), tensile, flexural and interlaminar shear properties were tested (loading rate and sample size were in accordance with the PRC National Testing Standards GB/T 3354-2014, GB/T 3356-2014 and GB/T 30969-2014). All characterization and mechanical tests were performed at room temperature (25°C) and standard humidity (50%-70%). For each kind of mechanical tests, five laminate samples were used respectively. Calculation method of mechanical tests, results statistics and test conditions were introduced as follows:

Tensile test

Loading rate was 2 mm/min. For thin strip style, the clamping end was used to clamp and load with friction force. Uniform tension field was formed in the style working section, and tensile properties were tested. Tensile strength was calculated by:

$$\sigma_t = \frac{P_{max}}{\omega h} \qquad \text{(Equation 1)}$$

σ_t —— Tensile strength, (MPa);

P_{max} —— Maximum load before failure, (N);

ω —— Width of the sample, (mm);

h —— Thickness of the sample, (mm).

Tensile modulus was calculated by:

$$E_t = \frac{\Delta P l}{\omega h \Delta l}$$

(Equation 2)

E_t —— Tensile modulus, (MPa);

l —— The sample length of the working section, (mm);

ΔP —— Load increment, (N);

Δl —— The deformation increment corresponding to ΔP.

The length of the sample should be more than 25 cm, the width ω was 25 ± 0.1 mm, and the thickness h was 2-4 mm.

Flexural test

Loading rate was 2 mm/min. For straight strip samples, three-point bending method was used to apply load, and the bending stress distribution field was applied in the middle of the sample to test the pattern bending performance. Flexural strength was calculated by:

$$\sigma_f = \frac{3 P_{max} L}{2 \omega h^2}$$

(Equation 3)

σ_f —— Flexural strength, (MPa);

P_{max} —— Maximum load before failure, (N);

L —— Span, (mm);

ω —— Width of the sample, (mm);

h —— Thickness of the sample, (mm).

Flexural modulus was calculated by:

$$E_f = \frac{\Delta \sigma}{\Delta \varepsilon}$$

(Equation 4)

E_f —— Flexural modulus, (MPa);

$\Delta \sigma$ —— The difference of bending stresses between two selected strain points, (MPa);

$\Delta \varepsilon$ —— The difference of bending strains between two selected strain points (mm/mm).

The length of the sample should be more than $(L+20)$ mm, the width ω was 25 ± 0.1 mm, and the thickness h was 2-4 mm, L was 32 times the thickness size.

Interlaminar shear test

For straight strip samples, the shear strength of short beam was obtained by using three-point bending method with small span to thickness ratio. ILSS was calculated by:

$$\tau_{sbs} = \frac{3 P_{max}}{4 \omega h}$$

(Equation 5)

τ_{sbs} —— ILSS, (MPa);

P_{max} —— Maximum load before failure, (N);

ω —— Width of the sample, (mm);

h —— Thickness of the sample, (mm).

Generally, according to the experience, interlaminar shear modulus was calculated by:

$$E_{sbs} = 0.425E_f \quad\quad \text{(Equation 6)}$$

E_{sbs} —— Interlaminar shear modulus, (MPa);

E_f —— Flexural modulus of short beam under three points bending, (MPa).

The length of the sample should be more than $(5h+10)$ mm, the thickness h was 2-6 mm, and the width was 2-3 times the thickness size.

Qualitative test of interface strength

First, a bundle of raw CFs, PDA-CFs and ZnO-PDA-CFs with equal length were taken, respectively. One end of these bundles were soaked in the epoxy resin by 3 mm. After curing, both ends of the fibers were tightened and a load was applied uniformly to pull the fiber bundle out of the resin. At least five bundles of each sample were used for interface strength test, respectively.

Fiber surface wettability test

Firstly, the raw CFs and modified CFs (PDA-CFs and ZnO-PDA-CFs) were filled into a straw with a diameter of about 3 mm. The length of fibers exposed from the straw was about 3 mm. The straw was suspended vertically from the support bar and the entire test rack was placed on the analytical balance. Then, the end of the straw was dipped into the epoxy vertically while the mass change shown by the analytical balance was recorded. In the process of resin infiltration, the mass of the fibers will gradually increase until reached a stable value. The data was recorded every second until the mass change was no longer noticeable. At least five bundles of each sample were used for fiber surface wettability test, respectively.